Ionics (2024) 30:4655–4664
https://doi.org/10.1007/s11581-024-05604-3

RESEARCH

Wedelia chinensis-derived biomass porous carbon as anode material for high performance sodium/potassium-ion batteries

Zengwei Pang[1] · Letong Wang[1] · Shenteng Wan[1] · Miaomiao Liu[1] · Xiaohui Niu[1] · Kunjie Wang[1] · Hongxia Li[1]

Received: 3 March 2024 / Revised: 18 April 2024 / Accepted: 25 May 2024 / Published online: 13 June 2024

Abstract

Sodium-ion batteries (SIBs) and potassium-ion batteries (PIBs) are potential alternatives of lithium-ion batteries (LIBs) due to the abundant and cost-effective availability of sodium and potassium resources. Unfortunately, they are difficult to use for large-scale grid energy storage due to the lack of suitable anode materials for sodium/potassium energy storage. Biomass-derived carbon, which is widely available and environmentally friendly, is one of the most promising anode materials for SIBs/PIBs, but the design and regulation of its microstructure is exceptionally complex. By selecting suitable biomass precursors, it is expected that biomass-derived carbon with suitable microstructures can be simply prepared. In this study, *Wedelia chinensis* were selected as biomass precursors, and biomass-derived carbon materials with large interfacial spacing, suitable pores and high-specific surface area were prepared by a simple one-step pyrolysis method. The material exhibited fast energy storage kinetics when electrochemically tested as an anode and showed different performance advantages in storing sodium/potassium. When tested as an anode for SIBs, it exhibited excellent specific capacity and cycling stability (380.7 mA h g^{-1} after 500 cycles at 100 mA g^{-1}); When tested as an anode for PIBs, it exhibited excellent rate performance (128.6 mA h g^{-1} at 10 A g^{-1}).

Keywords Sodium-ion batteries · Potassium-ion batteries · *Wedelia chinensis* · Biomass-derived carbon · Pore structure · Energy storage

Introduction

The development and utilization of green energy and renewable resources has received a great deal of attention in the past few decades due to the energy crisis caused by the over-exploitation of fossil fuels [1–3]. The practical application of green energy and renewable energy needs to be realized with energy storage technology [4, 5]. Electrochemical energy storage is dominant in many energy storage technologies due to its unique advantages of flexibility and reliability [6, 7]. LIBs have played a huge role in electrochemical energy storage field since they were commercialized more than 30 years ago [8]. However, low reserve and uneven distribution of lithium resource further hinder their application in the large-scale stationary energy storage [9, 10]. There is an urgent need to find new alternatives of LIBs. The SIBs and PIBs have been largely developed in recent years due to their lower production cost, abundant resources, and similar physicochemical properties to lithium [11–15]. Unfortunately, the large ionic radius (Na^+ 1.02 Å, K^+ 1.38 Å) severely hinder the Na^+ and K^+ diffusion kinetics behavior, which negatively affects the cycling performance and rate performance of the device [16–18]. During the charging/discharging process, the repeated embedding/de-embedding of Na^+/K^+ will very easily result in the fragmentation of the anode material, which will lead to the deterioration of the electrochemical reversibility [19, 20]. Therefore, the development of high-specific capacity anodes with structural stability and fast energy storage kinetics is the key to solving the problems faced by SIBs/PIBs.

Carbon is gradually becoming the most promising material for industrial applications due to its excellent physical and chemical stability [21], abundant sources, and low price [22]. Graphitic carbon has a high theoretical specific capacity (372 mA h g^{-1}) [23] and a layered structure that favors

✉ Kunjie Wang
Wangkj80@lut.edu.cn

✉ Hongxia Li
lhxwkj790425@lut.edu.cn

[1] School of Petrochemical Engineering, Lanzhou University of Technology, Lanzhou 730050, P. R. China

Li^+ embedding [24]. However, graphite is not a suitable choice for SIBs as it is difficult for Na^+ to embed in graphite layer. Although K^+ ions could intercalate into graphite to give a theoretical specific capacity of 278 mA h g^{-1}, a large volume expansion of 61% is experienced by graphite anode in the potassiation/depotassiation process due to the larger size of K^+, which results in relatively fast capacity decay and inferior cycling stability [25, 26].

Amorphous carbon has a large layer spacing and many pores/defects, which are favorable for embedding/de-embedding of Na^+/K^+ ions and accommodating volume changes during cycling [27, 28]. Among them, biomass-derived carbon anodes have received extensive attention and a great deal of research due to their advantages of low cost, easy availability, fast regeneration and environmental friendliness [29–31]. However, the fabrication of high-quality biomass-derived carbonaceous materials with suitable pores and specific surface areas (SSA) is usually too cumbersome for large-scale preparation [32, 33]. Therefore, there is an urgent need to find a biomass-derived carbonaceous material that is suitable for industrial preparation. The Spartina alterniflora Loiser-derived biomass carbon prepared by Huanyu Wei et al. [34] in a one-step process as an anode material for SIBs maintained a reversible capacity of 141.63 mAh g^{-1} after 1000 cycles. Zhenrui Wu et al. [35] investigated the electrochemical performance of lignin-derived biomass carbon when used as anode for PIBs. The reversible specific capacity of lignin-derived biomass carbon in PIBs was 300 mAh g^{-1} at a current density of 0.1 A g^{-1}, and 79% of capacity retention was obtained.

Wedelia chinensis is extremely strong in growth and adaptation and is widely distributed in Asia. In this study, *W. chinensis* was utilized as a carbon source for direct pyrolysis in order to achieve the goal of large-scale preparation of biomass carbon (Fig. 1). Structural characterization and electrochemical analysis showed that the *W. chinensis*-derived porous carbon (WDPC) with appropriate pores and suitable specific surface area can be used as anode materials for SIBs and PIBs, providing good rate performance and high-specific capacity. As an anode material in SIBs, WDPC maintains a high reversible specific capacity of 380.7 mA h g^{-1} after 500 cycles at 100 mA g^{-1} with a capacity retention of 97%. While in PIBs, WDPC also exhibits an excellent rate performance, maintaining a high-specific capacity of 128.6 mA h g^{-1} even at a high current density of 10 A g^{-1}. This low-cost carbon-based material prepared by one-step pyrolysis provides guidance for the development of SIBs and PIBs.

Experimental section

Preparation of WDPC materials

Collected *Wedelia chinensis* were thoroughly washed with deionized water followed by soaking in ethanol for 12 h. After sufficient drying, the pulverized raw material was annealed in a tube furnace at 800 ℃ under argon for 2 h. The obtained sample was denoted as WDPC.

Material characterization

The structure of the materials was determined by using X-ray diffraction (XRD, X'Pert Pro, Netherlands) with Cu Kα radiation ($\lambda = 1.5418$ Å) at a sweep speed of 10° min^{-1}. Field emission scanning electron microscopy (SEM, JSF-6700F, Japan) and transmission electron microscopy (TEM, JEOL JEM-2010, Japan) were used to observe the microscopic morphology of biomass carbon. The surface composition of the material was determined by Thermo Scientific Escalab 259Xi X-ray photoelectron spectroscopy (XPS). Laser Raman spectroscopy (Raman) was performed using an excitation wavelength of 532 nm (LabRAM HR Evolution Raman spectrometer). Micromeritics ASAP 2020 nitrogen adsorption/desorption tester was used to test the specific surface area and the pore size distribution of the materials.

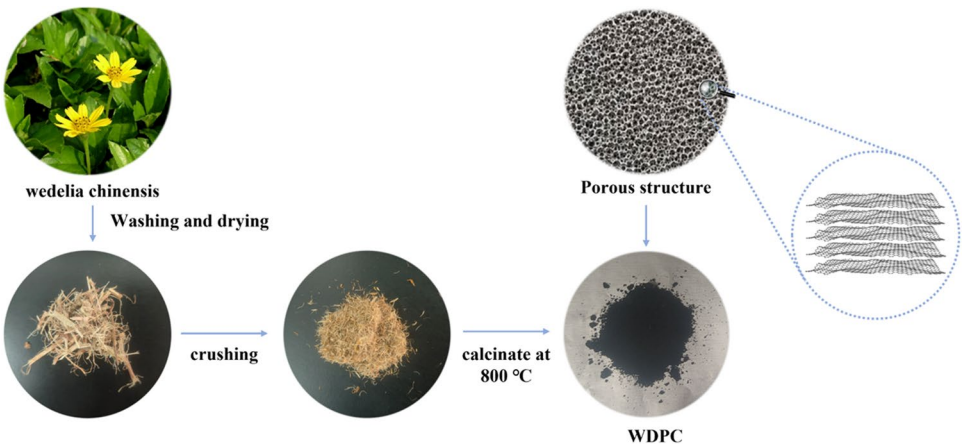

Fig. 1 Schematic illustration of the preparation of WDPC

Electrochemical measurement

The working electrode of the SIBs was prepared by thoroughly grinding and mixing the active material, acetylene black and polyvinylidene fluoride (PVDF) binder in N-methylpyrrolidone (NMP) with a mass ratio of 7:2:1. The above slurry was evenly coated on Cu foils that were dried at 110 ℃ for 12 h under vacuum. The loading density of active material was about 0.5 ~ 1.0 mg cm^{-2}. As for PIBs, the binder was sodium carboxymethyl cellulose (CMC), the other operations were the same as above. A series of CR2032 coin-type cells were assembled in a glove box filled with Ar (the content of H_2O and O_2 content < 0.01 ppm). The glass fibers (GF/D, Whatman) was used as separator, fresh sodium or potassium foil severed as counter electrode. The electrolyte was 1 M $NaClO_4$ in EC-PC (v:v = 1:1) and 0.8 M KPF_6 in EC-DEC (v:v = 1:1), respectively. Galvanostatic charge/discharge (GCD) curves, cycling performance, and galvanostatic intermittent titration technique (GITT) tests were performed on a battery test system (LAND CT2001) with a voltage window of 0.01–3 V. Cyclic voltammetry (CV) measurements were performed on an electrochemical workstation (CHI 760E).

Results and discussion

Morphology and structural features of material

Figure 2a–b displays the SEM images of the WDPC sample at different magnifications. It can be seen that WDPC is an irregular blocky morphology with abundant pores on the surface. The presence of these pores opens up channels for ions transfer and increases the active sites, which can play a positive role in the electrochemical properties of the material [36, 37]. The HRTEM images show the typical amorphous feature of WDPC. The SAED pattern does not show the diffraction spots of the crystals, again indicating the amorphous structure of WDPC.

In order to further investigate the structural properties, the material was characterized by XRD (Fig. 3a). It can be seen that the characteristic diffraction peak at 26° corresponding to the (002) crystal plane in the graphite structure becomes broader, weaker and shifts to a lower angle (~ 22°), which indicates a decrease in the degree of crystallinity of the carbon material and an increase in the spacing between the layers [38, 39]. According to the Bragg's equation, the (002) crystal plane spacing is found to be 0.376 nm. Larger lattice spacing facilitates rapid insertion and extraction of alkali metal ions to overcome high-energy diffusion barriers [40]. The characteristic diffraction peak at 43° corresponding to the (101) crystal plane almost disappears, further indicating that the carbon material structure tends to be disordered [41, 42]. The Raman spectrum of the WDPC material is shown in Fig. 3b. Two peaks at 1340 and 1595 cm^{-1} correspond to the D and G band of the carbon, respectively. The intensity ratio of I_{D1}/I_G is 0.94, indicating a low degree of graphitization. The specific surface area and pore size distribution of the materials were analyzed using N_2 adsorption/desorption isotherm. As can be seen in Fig. 3c, the high nitrogen adsorption at $P/P_0 < 0.05$ indicates that there is a large amount of micropores in the material. Moreover, there is a smaller H4-type hysteresis loop in the relative pressure interval of $0.45 < P/P_0 < 0.98$, indicating that there is also a certain amount of mesoporous structure in the material (Fig. 3d). The WDPC material has suitable specific surface area and porosity (374.94 $m^2\ g^{-1}$ and 0.26 $cm^3\ g^{-1}$). Generally, the high-specific surface area and ample pore structure are favorable of the ion transfer and the increase of active sites, which greatly improve the electrochemical performance of the materials. However, it is not conducive to the improvement of the initial Coulombic efficiency (ICE) because of more irreversible parasitic reactions [43]. XPS determines the elemental composition and state on the material surface. Only two elements, carbon and oxygen, were detected in the XPS survey scan. The oxygen content is 9.34%, which indicates that the material structure contains more oxygen-containing functional groups and more defects. In addition, the doping of heteroatoms can improve the

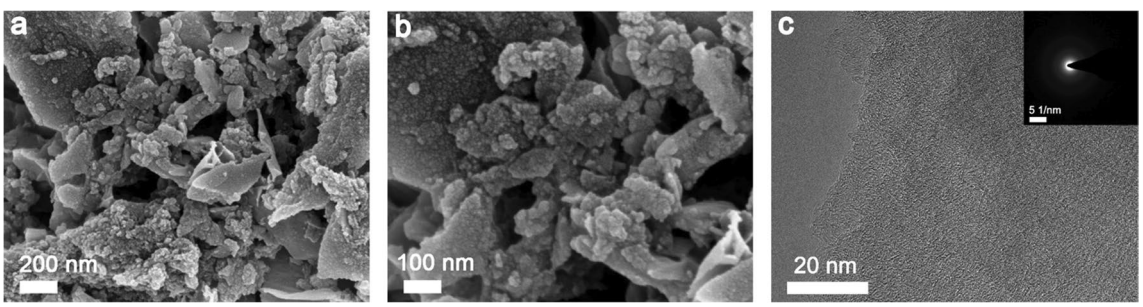

Fig. 2 **a**, **b** SEM images, **c** HRTEM image, and selected area electron diffraction (SAED) pattern of WDPC sample

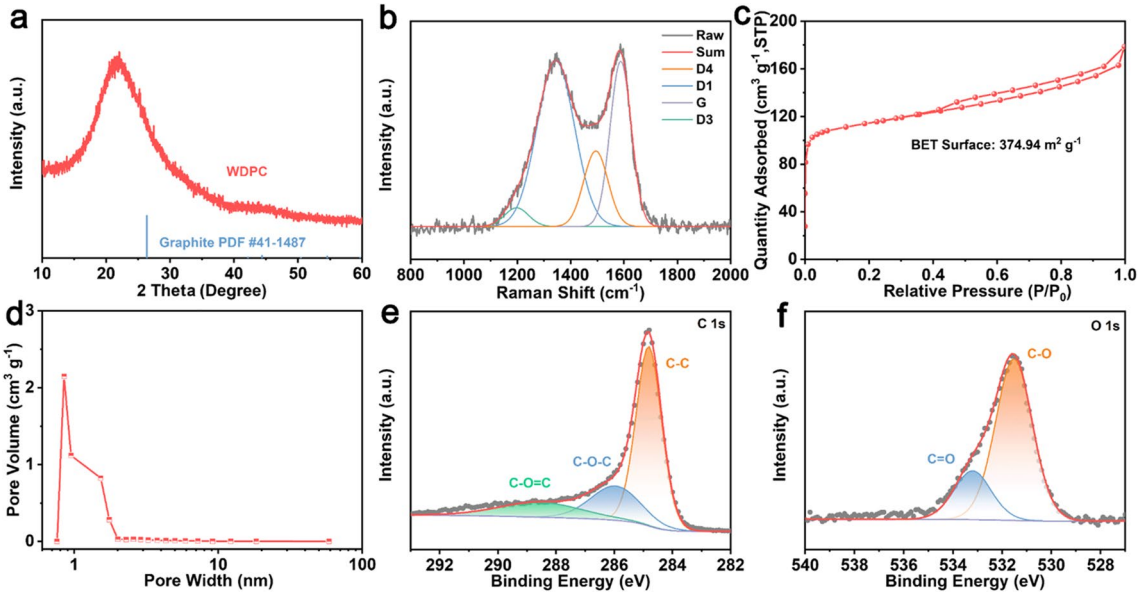

Fig. 3 **a** XRD pattern; **b** Raman spectra; **c** nitrogen adsorption–desorption isotherms; **d** pore size distribution plot; **e** C1s; **f** O1s XPS spectra of WDPC sample

wettability of the carbon material and increase the contact between the electrolyte and the electrode [44, 45]. The diffusion and transport distances of ions and electrons are also shortened, which is beneficial for improving the material rate performance [46]. High-resolution C1s and O1s XPS spectra of the WDPC sample are presented in Fig. 3e–f. The high-resolution C1s spectrum can be deconvoluted into three peaks at 284.8, 286, and 288.8 eV, corresponding to C–C, C–O–C, and C-O=C, respectively [47]. Similarly, the O1s spectrum can be decomposed into two peaks (Fig. 3f), which are also assigned to C-O (531.6 eV) and C=O (533.2 eV) in different ratios, respectively [48].

The electrochemical performance of WDPC as for anode material of SIBs/PIBs

The sodium/potassium ions storage performance of the WDPC electrode is investigated in a half-cell with Na/K metal as the counter electrode. In order to investigate the energy storage behavior of WDPC material, the CV curves were tested at different scan rates within an electrochemical window of 0.01–3 V. As shown in Fig. 4a–b, with the increase of scan rate, the shape of CV curves did not change too much except the potential of sodium ion intercalation/deintercalation is slightly shifted to a higher potential. This fully demonstrates the high reversibility and fast kinetic properties of the electrochemical reaction [49]. Since SIBs and PIBs have the same energy storage mechanism, the CV curves of PIBs is basically similar to that of SIBs. However, the integration area of CV curve in PIBs is slightly smaller than that of SIBs (at 0.3 mV s^{-1}, SIBs: 0.364 and PIBs: 0.302) due to the larger radius of K^+ ions, consequently making the intercalation/deintercalation of K^+ into the interfacial layer of the same carbon-based material relatively more difficult. It can also be seen from the CV curves that the intercalation/deintercalation potential of potassium ions in WDPC is higher than sodium ions. Therefore, from the safety point of view, PIBs have higher safety than SIBs [50, 51]. For the SIBs, the initial discharge/charge capacity was 647.9 mA h g^{-1}/308.2 mA h g^{-1} at 0.1 A g^{-1} (Fig. 4c), corresponding to 47.6% of ICE. The ICE is relatively low due to the occurrence of irreversible side reactions, including the irreversible decomposition of electrolyte and the accelerated growth of SEI [52]. Except for the irreversible discharge loss in the first cycle, the GCD curves show slope characteristics without obvious plateau, indicating good electrochemical kinetic behavior of the material [53]. The GCD curves almost overlap in the subsequent cycles, suggesting that the electrochemical processes at the WDPC electrode are highly reversible. The GCD curve of PIBs at 0.1 A g^{-1} is similar to that of SIBs, demonstrating a fast kinetic behavior in PIBs. The poor reproducibility of the GCD curves for PIBs is attributed to the higher reactivity of K^+ and the increased chance of side reactions on the electrode surface, which will cause significant decay of the specific capacity (Fig. 4d) [54]. Therefore, it is particularly important to precisely regulate the microstructure of anode materials in PIBs. SIBs and PIBs are subjected to rate performance tests at different current densities, and the results are shown in Fig. 4e. The discharge-specific capacities of WDPC in SIBs are 320.7, 246.4, 191, 147.7, 95.8, 75.7, and 68.4 mA h g^{-1} at current densities of 0.1, 0.2, 0.5, 1, 2, 5, and 10 A g^{-1}. When the

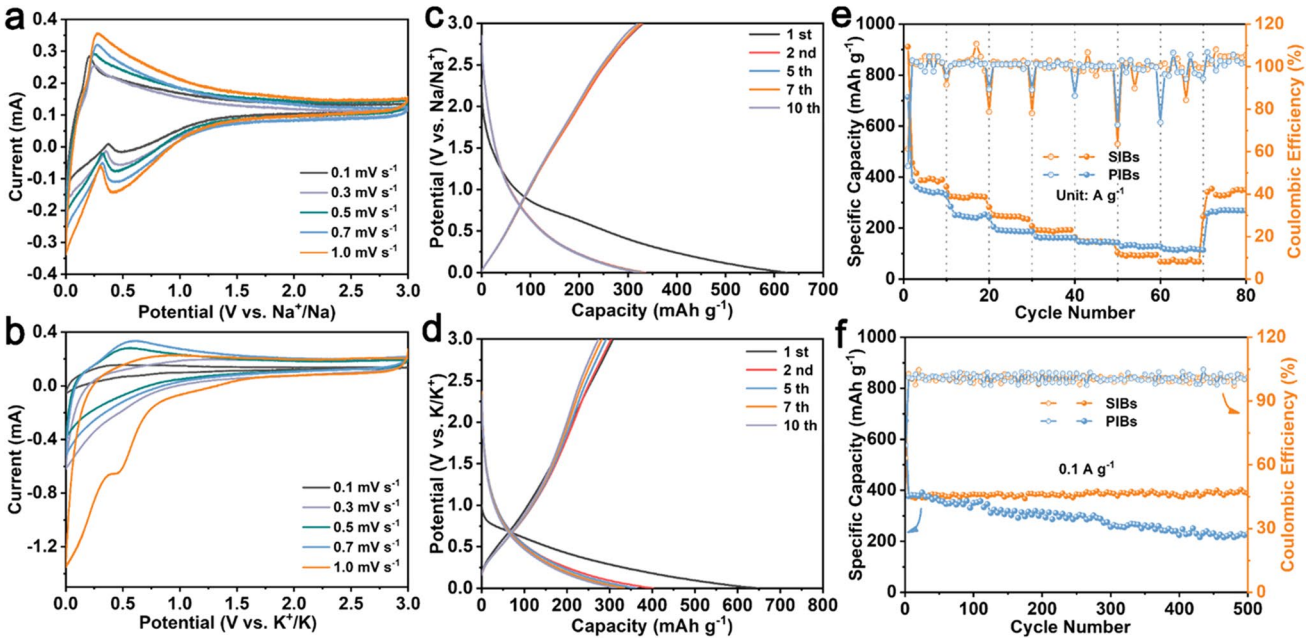

Fig. 4 The CV curves of WDPC anode electrode material at different scan rates: **a** SIBs, **b** PIBs respectively; GCD plots at 0.1 A g^{-1} of WDPC anode electrode material: **c** SIBs **d** PIBs respectively; **e** rate capability and **f** cyclic performance at 0.1 A g^{-1} of WDPC anode electrode material

current density is restored to 0.1 A g^{-1}, the discharge specific capacity is returned to 331.8 mA h g^{-1}, showing good reversibility and structural tolerance. The electrochemical properties of WDPC in PIBs are slightly different from those of SIBs. The specific capacity is significantly lower than that of SIBs at low current densities. The specific capacity decays more seriously at 0.1 A g^{-1}, which is consistent with that showed by the GCD curves. However, the typical features such as the smaller solvation radius [55], lower solvation energy, and fast ion transport properties of potassium ions [56] are beneficial to boost the ion transport kinetic behavior, finally resulting in the superior rate capabilities. Hence, the specific capacity decay in PIBs becomes much slower than SIBs with the increase of the current density. At the high current density of 10 A g^{-1}, as high as 128.6 mA h g^{-1} of specific capacity still can be achieved by WDPC anode in PIBs, displaying superior rate performance. Figure 4f demonstrates the cycling performance of WDPC in SIBs and PIBs. At a current density of 0.1 A g^{-1}, the WDPC displays a specific capacity of 380.7 mAh g^{-1} with essentially no capacity degradation, and Coulombic efficiency is nearly to 100% after 500 cycles in the SIBs system. However, in the PIBs system, the cycling stability is relatively poor and the Coulombic efficiency fluctuates obviously. This is mainly due to the repeated intercalation/deintercalation of larger potassium ions between the carbon layers of WDPC, leading to a more serious volume change.

In order to reveal the nature of the excellent electrochemical properties of WDPC material, its electrochemical energy storage kinetic behavior was investigated. The CV curves of the WDPC electrodes were tested at different sweep rates. According to the relationship showed in Eqs. (1), log(i) versus log(v) at different voltages are plotted separately, and the b values at different potentials can be obtained from the slopes of the straight lines [57, 58].

$$i = av^b \tag{1}$$

$$i = k_1 v + k_2 v^{1/2} \tag{2}$$

As shown in Fig. 5a, d, in both SIBs and PIBs, the b values are between 0.5 and 1 but not lower than 0.7, indicating that the charge storage is contributed by both a surface-driven behavior and a diffusion-controlled process, but the current response is mainly stemmed from the fast surface capacitance–controlled process (Fig. 5d). Semi-quantitative calculations based on Eq. (2) show that the charge storage mainly originates from diffusion-controlled processes at low scan rate (Fig. 5b, e). As the scan rate increases, the electrolyte ions diffuse at a slower rate and the diffusion-controlled process contributes progressively less to the charge storage (Fig. 5c, f). In particular, the radius of K^+ ion is larger than Na^+, the contribution of the diffusion-controlled process is reduced more significantly (Fig. 5f). The above results demonstrate that WDPC anode material with abundant pore structure has fast kinetic behaviors, and the ions transfer kinetic behavior dominated by surface capacitance-controlled processes during the charging and discharging

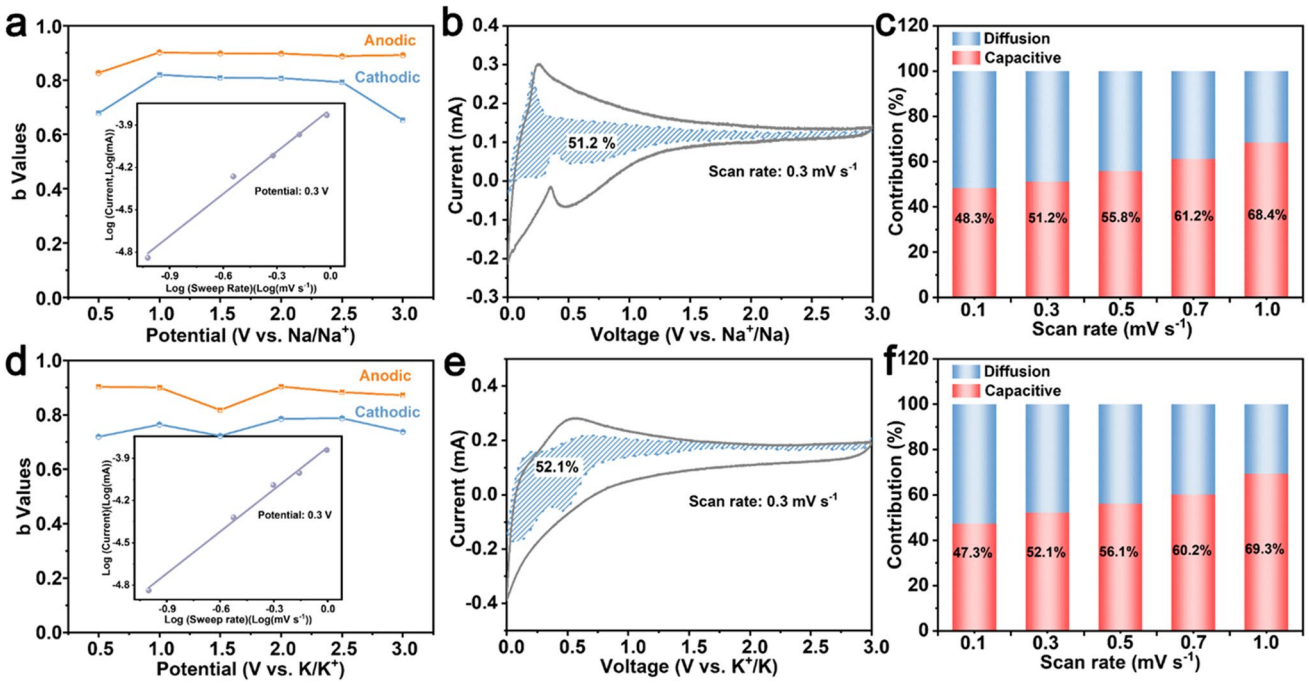

Fig. 5 **a, d** *b* values in SIBs and PIBs respectively; capacitive contribution ratios **b**, **e** at scan rate of 0.3 mV s^{-1} and **c**, **f** at different scan rate in SIBs and PIBs, respectively

processes. The superior kinetic behavior is inextricably linked to the microstructure and composition of the material, such as reasonable pore size distribution, large layer spacing, abundant active sites, and heteroatom doping.

The fast diffusion kinetic behavior of the WDPC anode was confirmed in measurements by the constant-current intermittent titration technique (GITT) and EIS as shown in Fig. 6. A simplified form of Fick's second law is used to calculate the diffusion coefficient of sodium/potassium ions with the equation as shown in follows [59, 60]:

$$D_{K^+} = \frac{4}{\pi\tau}\left(\frac{m_B V_M}{M_B A}\right)^2\left(\frac{\Delta E_s}{\Delta E_\tau}\right)^2 \quad (3)$$

In the equation, m_B, V_M, and M_B are the mass (g), molar volume (L mol^{-1}) and molar mass (g mol^{-1}) of the active substance, respectively. A is the geometric contact area between the electrode material and the electrolyte. τ is the constant current pulse time, ΔE_τ is the total transient potential change in time τ due to the application of constant current I, and ΔE_S is the change in the steady-state voltage of the cell due to the application of the constant current I. The cell voltage change in time τ is the change in the steady-state voltage of the electrode material. For the WDPC anode materials, the trends of overpotential changes in SIBs and PIBs are basically the same. During the charging process, the overpotential gradually increases. The overpotential decreases as the degree of discharge increases [61]. According to Fick's second law calculation, D_{Na+} varies in the range of $4.58\times10^{-10}\sim1.12\times10^{-12}$ cm^2 s^{-1} during charging and discharging process, while D_{K+} varies in the range of $7.12\times10^{-11}\sim5.21\times10^{-13}$ cm^2 s^{-1} (Fig. 6b, d). Apparently, the ion diffusion rate decreases with the increase of metal ion radius, which is also closely related to the difficulty of the ions embedding into the carbon material interlayer.

The Nyquist plots are shown in Fig. 6e–g and fitted by an equivalent circuit in the inset of Fig. 6e. Nyquist plots of SIBs and PIBs show the similar variation tendency in the whole process. Specifically, the charge transfer resistance (R_{ct}) drastically decreases after cycling and keeps almost constant during subsequent cycles, suggesting the stable charge transfer behaviors on the electrode/electrolyte interface [62]. This is mainly ascribed to the promotion of the electrolyte wettability of the material during the initial cycles, and the formation of the stable SEI layer after cycling [63, 64]. The R_{ct} of SIBs is fitted to about 63.5 Ω, smaller than that in PIBs (117.6 Ω), and is beneficial for obtaining fast ion transport and charge transfer process. A larger slope at low frequency in SIBs suggests that the faster sodium ion diffusion in WDPC electrode, which are ascribed to the smaller sodium ion radius than potassium ion (Fig. 6g).

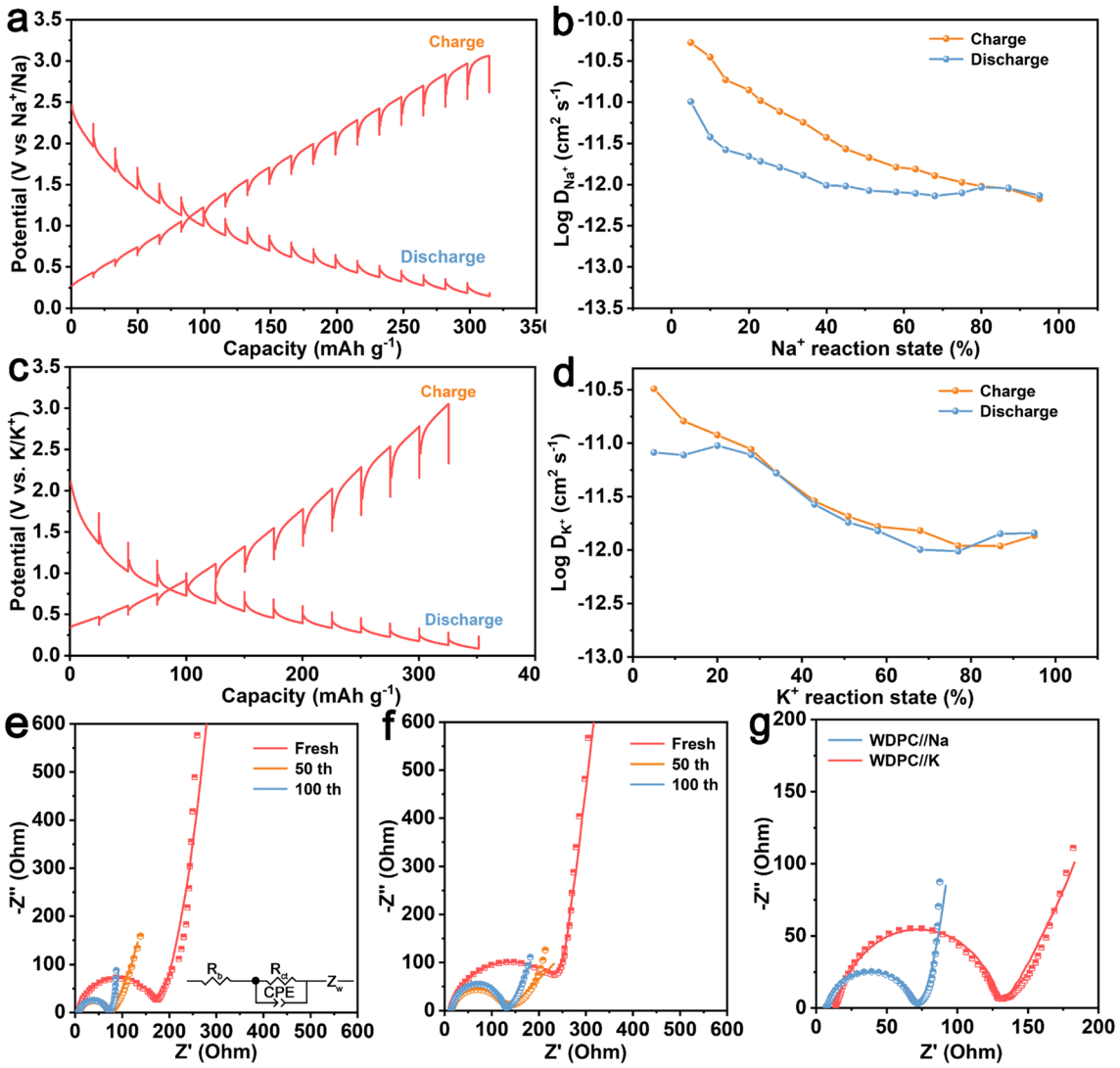

Fig. 6 GITT plots in **a, c** SIBs and PIBs, respectively; ion diffusion coefficients in **b, d** of SIBs and PIBs, separately; Nyquist plots of **e** SIBs, **f** PIBs at different cycles. **g** Nyquist plots after 100 cycles

Conclusion

In this work, with the aim of simple preparation of high-performance carbon anode materials for SIBs/PIBs, biomass-derived carbon materials with suitable specific surface area and rich pore structure were prepared by selecting *Wedelia chinensis* as the biomass carbon source. The sodium/potassium storage properties of the material were investigated by GCD and rate performance testing. The relationships between the electrochemical properties of the material and the structure (the lattice spacing, the specific surface area, the pore structure and the surface functional groups) were clarified. The kinetic behavior of the material for energy storage was also deeply investigated. Benefiting from the moderate-specific surface area, abundant pore structure and larger interfacial spacing of WDPC, a high reversible–specific capacity and a long cycling performance were achieved in both SIBs and PIBs. The WDPC is expected to be a potential anode candidate for the next-generation high-performance SIBs and PIBs.

Acknowledgements Zengwei Pang and Letong Wang contributed equally to this work.

Author contributions Kunjie Wang: Conceptualization, project management;

Zengwei Pang: Writing the paper, preparing samples, testing statistics;

Letong Wang: Investigation;

Shenteng Wan: Software, resources;

Miaomiao Liu: Validation, formal analysis;

Xiaohui Niu: Data organization, supervision;

Hongxia Li: Visualization., Writing the paper, formal analysis.

Funding This work was supported by the National Nature Science Foundation of China (22065021), the Key Research Program of Gansu Province (21YF5GA076), the Province Nature Science Foundation of Gansu (21JR7RA213) and Hongliu Outstanding Youth Teacher Cultivate Project of Lanzhou University of Technology.

Data availability No datasets were generated or analysed during the current study.

Declarations

Competing interests The authors declare no competing interests.

References

1. Yue X, Qiao B, Wang J, Xie Z, Liu Z, Yang Z, Abudula A, Guan G (2023) Layered metal chalcogenide based anode materials for high performance sodium ion batteries: a review. Renew Sust Eenrg Rev 185:113592. https://doi.org/10.1016/j.rser.2023.113592
2. Singh AN, Islam M, Meena A, Faizan M, Han D, Bathula C, Hajibabaei A, Anand R, Nam KW (2023) Unleashing the potential of sodium-ion batteries: current state and future directions for sustainable energy storage. Adv Funct Mater 33(46):2304617. https://doi.org/10.1002/adfm.202304617
3. Hirsh HS, Li Y, Tan DH, Zhang M, Zhao E, Meng YS (2020) Sodium-ion batteries paving the way for grid energy storage. Adv Energy Mater 10(32):2001274. https://doi.org/10.1002/aenm.202001274
4. Huang Z-X, Gu Z-Y, Heng Y-L, Ang EH, Geng H-B, Wu X-L (2023) Advanced layered oxide cathodes for sodium/potassium-ion batteries: development, challenges and prospects. Chem Eng J 452(3):139438. https://doi.org/10.1016/j.cej.2022.139438
5. Li J, Zhang W, Zheng W (2023) Metal selenides find plenty of space in architecting advanced sodium/potassium ion batteries. Small 20(4):2305021. https://doi.org/10.1002/smll.202305021
6. Dai C, Jin X, Ma H, Hu L, Sun G, Chen H, Yang Q, Xu M, Liu Q, Xiao Y (2021) Maximizing energy storage of flexible aqueous batteries through decoupling charge carriers. Adv Energy Mater 11(14):2003982. https://doi.org/10.1002/aenm.202003982
7. Wang W, Yuan B, Sun Q, Wennersten R (2022) Application of energy storage in integrated energy systems—a solution to fluctuation and uncertainty of renewable energy. J Energy Storage 52(A):104812. https://doi.org/10.1016/j.est.2022.104812
8. Shin J, Choi JW (2020) Opportunities and reality of aqueous rechargeable batteries. Adv Energy Mater 10(28):2001386. https://doi.org/10.1002/aenm.202001386
9. Li X, Wang Y, Wu J, Tong L, Wang S, Li X, Chen Y (2023) Engineering contact curved interface with high-electronic-state active sites for high-performance potassium-ion batteries. PNAS 120(52):e2307477120. https://doi.org/10.1073/pnas.2307477120
10. Chen X, Tong L, He J, Yuan Z, Wang Y, Li X, Li M, Wang M, Wu J, Chen Y, Li X (2023) Cow leather-derived N/O codoped hard carbon as a high-performance anode material for sodium-ion batteries. Mater Today Commun 37:107361. https://doi.org/10.1016/j.mtcomm.2023.107361
11. Zhao Y, Kang Y, Wozny J, Lu J, Du H, Li C, Li T, Kang F, Tavajohi N, Li B (2023) Recycling of sodium-ion batteries. Nat Rev Mater 8:623–634. https://doi.org/10.1038/s41578-023-00574-w
12. Zuo W, Innocenti A, Zarrabeitia M, Bresser D, Yang Y, Passerini S (2023) Layered oxide cathodes for sodium-ion batteries: storage mechanism, electrochemistry, and techno-economics. Acc Chem Res 56(3):284–296. https://doi.org/10.1021/acs.accounts.2c00690
13. Yu T, Li G, Duan Y, Wu Y, Zhang T, Zhao X, Luo M, Liu Y, Compounds (2023) The research and industrialization progress and prospects of sodium ion battery. J Alloy Compd 958(5):170486. https://doi.org/10.1016/j.jallcom.2023.170486
14. Ji B, Yao W, Zheng Y, Kidkhunthod P, Zhou X, Tunmee S, Sattayaporn S, Cheng H-M, He H, Tang Y (2020) A fluoroxalate cathode material for potassium-ion batteries with ultra-long cyclability. Nat commun 11:1225. https://doi.org/10.1038/s41467-020-15044-y
15. Hu R, Tong Y, Yin J, Wu J, Zhao J, Cao D, Zhu K (2024) Dual carbon engineering enabling 1T/2H MoS_2 with ultrastable potassium ion storage performance. Nanoscale Horiz Nanoscale Horiz 9(2):305–316. https://doi.org/10.1039/d3nh00404j
16. Dudev T, Lim C (2010) Factors governing the Na^+ vs K^+ selectivity in sodium ion channels. J Am Chem Soc 132(7):2321–2332. https://doi.org/10.1021/ja909280g
17. Liang X, Hwang JY, Sun YK (2023) Practical cathodes for sodium-ion batteries: who will take the crown? Adv Energy Mater 13(37):2301975. https://doi.org/10.1002/aenm.202301975
18. Wu J, He J, Wang M, Li M, Zhao J, Li Z, Chen Y (2023) Electrospun carbon-based nanomaterials for next-generation potassium batteries. Chem Commun 59(17):2381–2398. https://doi.org/10.1039/d2cc06692k
19. Xiao S, Li X, Li T, Xiang Y, Chen JS (2021) Practical strategies for enhanced performance of anode materials in Na^+/K^+-ion batteries. J Mate Chem A 9:7317–7335. https://doi.org/10.1039/d0ta12417f
20. Shao R, Sun Z, Wang L, Pan J, Yi L, Zhang Y, Han J, Yao Z, Li J, Wen Z (2024) Resolving the origins of superior cycling performance of antimony anode in sodium-ion batteries: a comparison with lithium-ion batteries. Angew Chem e202320183. https://doi.org/10.1002/ange.202320183
21. Xie L, Tang C, Bi Z, Song M, Fan Y, Yan C, Li X, Su F, Zhang Q, Chen C (2021) Hard carbon anodes for next-generation li-ion batteries: review and perspective. Adv Energy Mater 11(38):2101650. https://doi.org/10.1002/aenm.202101650
22. Zhang X, Huang R, Wu F, Chen R, Li L (2023) Mixed-biomass engineering achieves multi-doped highly-disordered hierarchical flower-like hard carbon for advanced potassium-ion battery. Nano Energy 117:108913. https://doi.org/10.1016/j.nanoen.2023.108913
23. Zheng Z, Hu S, Yin W, Peng J, Wang R, Jin J, He B, Gong Y, Wang H, Fan HJ (2024) CO_2-etching creates abundant closed pores in hard carbon for high-plateau-capacity sodium storage. Adv Energy Mater 14(3):2303064. https://doi.org/10.1002/aenm.202303064
24. Chen J, Mao Z, Zhang L, Wang D, Xu R, Bie L, Fahlman BD (2017) Nitrogen-deficient graphitic carbon nitride with enhanced performance for lithium ion battery anodes. ACS Nano 11(12):12650–12657. https://doi.org/10.1021/acsnano.7b07116
25. Xiao B, Zhang H, Sun Z, Li M, Fan Y, Lin H, Zhang Q (2023) Achieving high-capacity and long-life K^+ storage enabled by constructing yolk-shell Sb_2S_3@ N, S-doped carbon nanorod anodes. J Energy Chem 76:547–556. https://doi.org/10.1016/j.jechem.2022.09.050
26. He XX, Lai WH, Liang Y, Zhao JH, Yang Z, Peng J, Liu XH, Wang YX, Qiao Y, Li L (2023) Achieving all-plateau and high-capacity sodium insertion in topological graphitized carbon. Adv Mater 35(40):2302613. https://doi.org/10.1002/adma.202302613
27. Toh C-T, Zhang H, Lin J, Mayorov AS, Wang Y-P, Orofeo CM, Ferry DB, Andersen H, Kakenov N, Guo Z (2020) Synthesis and properties of free-standing monolayer amorphous carbon. Nature 577:199–203. https://doi.org/10.1038/s41586-019-1871-2
28. Zhang H, Li W, Pan J, Sun Z, Xiao B, Ye W, Ke C, Gao H, Cheng Y, Zhang QJ (2022) Synergistic coupling of amorphous carbon and graphitic domains toward high-rate and long-life K^+ storage. J

Energy Chem 73:533–541. https://doi.org/10.1016/j.jechem.2022.07.004
29. Park S, Song J, Lee WC, Jang SH, Lee J, Kim J, Kim H-K, Min K (2023) Advances in biomass-derived electrode materials for energy storage and circular carbon economy. Chem Eng J 470(15):144234. https://doi.org/10.1016/j.cej.2023.144234
30. He H, Zhang R, Zhang P, Wang P, Chen N, Qian B, Zhang L, Yu J, Dai B (2023) Functional carbon from nature: biomass-derived carbon materials and the recent progress of their applications. Adv Sci 10(16):2205557. https://doi.org/10.1002/advs.202205557
31. Hernández-Rentero C, Marangon V, Olivares-Marín M, Gómez-Serrano V, Caballero Á, Morales J, Hassoun J (2020) Alternative lithium-ion battery using biomass-derived carbons as environmentally sustainable anode. J Colloid Interf Sci 573(1):396–408. https://doi.org/10.1016/j.jcis.2020.03.092
32. Sun Y, Shi XL, Yang YL, Suo G, Zhang L, Lu S, Chen ZG (2022) Biomass-derived carbon for high-performance batteries: from structure to properties. Adv Funct Mater 32(24):2201584. https://doi.org/10.1002/adfm.202201584
33. Malode SJ, Shanbhag MM, Kumari R, Dkhar DS, Chandra P, Shetti NP (2023) Biomass-derived carbon nanomaterials for sensor applications. J Pharmaceut Biomed 222(5):115102. https://doi.org/10.1016/j.jpba.2022.115102
34. Wei H, Cheng H, Yao N, Li G, Du Z, Luo R, Zheng Z (2023) Invasive alien plant biomass-derived hard carbon anode for sodium-ion batteries. Chemosphere 343:140220. https://doi.org/10.1016/j.chemosphere.2023.140220
35. Wu Z, Zou J, Zhang Y, Lin X, Fry D, Wang L, Liu J (2022) Lignin-derived hard carbon anode for potassium-ion batteries: interplay among lignin molecular weight, material structures, and storage mechanisms. Chem Eng J 427(1):131547. https://doi.org/10.1016/j.cej.2021.131547
36. Kim J, Park J, Lee J, Lim WG, Jo C, Lee J (2021) Biomass-derived P, N self-doped hard carbon as bifunctional oxygen electrocatalyst and anode material for seawater batteries. Adv Funct Mater 31(22):2010882. https://doi.org/10.1002/adfm.202010882
37. Zhu Z, Zhong W, Zhang Y, Dong P, Sun S, Zhang Y, Li X (2021) Elucidating electrochemical intercalation mechanisms of biomass-derived hard carbon in sodium-/potassium-ion batteries. Carbon Energy 3(4):541–553. https://doi.org/10.1002/cey2.111
38. Zhong L, Qiu X, Yang S, Sun S, Chen L, Zhang W (2023) Supermolecule-regulated synthesis strategy of general biomass-derived highly nitrogen-doped carbons toward potassium-ion hybrid capacitors with enhanced performances. Energy Storage Mater 61:102887. https://doi.org/10.1016/j.ensm.2023.102887
39. Saikia D, Deka JR, Lu B-J, Chen Y-C, Lian J-W, Kao H-M, Yang Y-C (2023) Pinecone-derived biomass carbons as anodes for lithium and sodium-ion batteries by template-assisted and chemically activated approaches. J Power Sources 580(1):233329. https://doi.org/10.1016/j.jpowsour.2023.233329
40. Xu Y, Bahmani F, Zhou M, Li Y, Zhang C, Liang F, Kazemi SH, Kaiser U, Meng G, Lei Y (2019) Enhancing potassium-ion battery performance by defect and interlayer engineering. Nanoscale Horiz 4:202–207. https://doi.org/10.1039/c8nh00305j
41. Li Z, Chen Y, Jian Z, Jiang H, Razink JJ, Stickle WF, Neuefeind JC, Ji X (2018) Defective hard carbon anode for Na-ion batteries. Chem Mater 30(14):4536–4542. https://doi.org/10.1021/acs.chemmater.8b00645
42. Qin D, Wang L, Zeng X, Shen J, Huang F, Xu G, Zhu M, Dai Z (2023) Tailored edge-heteroatom tri-doping strategy of turbostratic carbon anodes for high-rate performance lithium and sodium-ion batteries. Energy Storage Mater 54:498–507. https://doi.org/10.1016/j.ensm.2022.10.049
43. Yang S, Dong W, Shen D, Li S, Sun W, Hong X, Wang M, Mao Y (2017) Composite of nonexpansion reduced graphite oxide and carbon derived from pitch as anodes of Na-ion batteries with high coulombic efficiency. Chem Eng J 309(1):674–681. https://doi.org/10.1016/j.cej.2016.10.074
44. Gao J, Wang G, Wang W, Yu L, Peng B, El-Harairy A, Li J, Zhang G (2022) Engineering electronic transfer dynamics and ion adsorption capability in dual-doped carbon for high-energy potassium ion hybrid capacitors. ACS Nano 16(4):6255–6265. https://doi.org/10.1021/acsnano.2c00140
45. Jin Q, Wang K, Feng P, Zhang Z, Cheng S, Jiang K (2020) Surface-dominated storage of heteroatoms-doping hard carbon for sodium-ion batteries. Energy Storage Mater 27:43–50
46. Qiu C, Jiang L, Gao Y, Sheng L (2023) Effects of oxygen-containing functional groups on carbon materials in supercapacitors. Mater Des 111952. https://doi.org/10.1016/j.matdes.2023.111952
47. Xu T, Qiu X, Zhang X, Xia Y (2023) Regulation of surface oxygen functional groups and pore structure of bamboo-derived hard carbon for enhanced sodium storage performance. Chem Eng J 452(4):139514. https://doi.org/10.1016/j.cej.2022.139514
48. Kim M, Fernando JF, Li Z, Alowasheeir A, Ashok A, Xin R, Martin D, Nanjundan AK, Golberg DV, Yamauchi Y (2022) Ultrastable sodium ion storage of biomass porous carbon derived from sugarcane. Chem Eng J 445(1):136344. https://doi.org/10.1016/j.cej.2022.136344
49. Zhang Y, Jiang S, Li Y, Ren X, Zhang P, Sun L, Yang HY (2023) In situ grown hierarchical electrospun nanofiber skeletons with embedded vanadium nitride nanograins for ultra-fast and super-long cycle life aqueous Zn-ion batteries. Adv Energy Mater 13(5):2202826. https://doi.org/10.1002/aenm.202202826
50. Liu M, Wang Y, Wu F, Bai Y, Li Y, Gong Y, Feng X, Li Y, Wang X, Wu C (2022) Advances in carbon materials for sodium and potassium storage. Adv Funct Mater 32(31):2203117. https://doi.org/10.1002/adfm.202203117
51. Xiao K, Wu J-F, Yan H, Mo Y, Zhou W, Peng Y, Chen S, Cui X, Chen L, Xu C, Liu J (2022) Intercalation-deposition mechanism induced by aligned carbon fiber toward dendrite-free metallic potassium batteries. Energy Storage Mater 51:122–129. https://doi.org/10.1016/j.ensm.2022.06.033
52. Cheng D, Li Z, Zhang M, Duan Z, Wang J, Wang C (2023) Engineering ultrathin carbon layer on porous hard carbon boosts sodium storage with high initial coulombic efficiency. ACS Nano 17(19):19063–19075. https://doi.org/10.1021/acsnano.3c04984
53. Li H, Lang J, Lei S, Chen J, Wang K, Liu L, Zhang T, Liu W, Yan X (2018) A high-performance sodium-ion hybrid capacitor constructed by metal–organic framework–derived anode and cathode materials. Adv Funct Mater 28(30):1800757. https://doi.org/10.1002/adfm.201800757
54. Zhang E, Wu S, Sun X, Wang B, Xu L, Yi X, Wang X, Lu B (2023) Iron carbodiimide as a high-reactivity anode for potassium ion batteries. Chem Eng J 453(2):139966. https://doi.org/10.1016/j.cej.2022.139966
55. Chen J, Lei S, Zhang S, Zhu C, Liu Q, Wang C, Zhang Z, Wang S, Shi Y, Yin L (2023) Dilute aqueous hybrid electrolyte with regulated core-shell-solvation structure endows safe and low-cost potassium-ion energy storage devices. Adv Funct Mater 33(19):2215027. https://doi.org/10.1002/adfm.202215027
56. Sada K, Darga J, Manthiram A (2023) Challenges and prospects of sodium-ion and potassium-ion batteries for mass production. Adv Energy Mater 13(39):2302321. https://doi.org/10.1002/adfm.202215027
57. Pan X, Xi B, Lu H, Zhang Z, An X, Liu J, Feng J, Xiong S (2022) Molybdenum oxynitride atomic nanoclusters bonded in nanosheets of N-doped carbon hierarchical microspheres for efficient sodium storage. Nano-Micro Lett 14:163. https://doi.org/10.1007/s40820-022-00893-7
58. Hu R, Sha D, Cao X, Lu C, Wei Y, Pan L, Sun Z (2022) Anchoring metal-organic framework-derived ZnTe@C onto elastic $Ti_3C_2T_x$ MXene with 0D/2D dual confinement for ultrastable

potassium-ion storage. Adv Energy Mater 12(47):2203118. https://doi.org/10.1002/aenm.202203118
59. Chen Z-X, Cheng Q, Li X-Y, Li Z, Song Y-W, Sun F, Zhao M, Zhang X-Q, Li B-Q, Huang J-Q (2023) Cathode kinetics evaluation in lean-electrolyte lithium–sulfur batteries. J Am Chem Soc 145(30):16449–16457. https://doi.org/10.1021/jacs.3c02786
60. Yao Y, Cumberbatch H, Robertson DD, Chin MA, Lamkin R, Tolbert SH (2023) On the interplay between size and disorder in suppressing intercalation-induced phase transitions in pseudocapacitive nanostructured MoS_2. Adv Funct Mater 2304896. https://doi.org/10.1002/adfm.202304896
61. Wi S, Park J, Lee S, Kim J, Gil B, Yun AJ, Sung Y-E, Park B, Kim C (2017) Insights on the delithiation/lithiation reactions of Li $Mn_{0.8}Fe_{0.2}PO_4$ mesocrystals in Li^+ batteries by in situ techniques. Nano Energy 39:371–379. https://doi.org/10.1016/j.nanoen.2017.07.016e
62. Chen S, Huang S, Zhang YF, Fan S, Yan D, Shang Y, Yang HY (2020) Constructing stress-release layer on Fe_7Se_8-based composite for highly stable sodium-storage. Nano Energy 69:104389. https://doi.org/10.1016/j.nanoen.2019.104389
63. Yan D, Li K, Yan Y, Huang S, Von Lim Y, Shang Y, Yang HY (2021) Cubic spinel XIn_2S_4 (X= Fe Co, Mn): a new type of anode material for superfast and ultrastable Na-ion storage. Adv Energy Mater 11(44):2102137. https://doi.org/10.1002/aenm.202102137
64. Ma P, Zhang Z, Wang J, Li H, Yang HY, Shi Y (2023) Self-assembled 2D $VS_2/Ti_3C_2T_x$ MXene nanostructures with ultrafast kinetics for superior electrochemical sodium-ion storage. Adv Sci 10(31):2304465. https://doi.org/10.1002/advs.202304465